Numerical Heat Transfer, Part B, 37:437–454, 2000

1040–7790/00 $12.00 + .00

AN ADAPTIVE LEVEL SET METHOD FOR MOVING-BOUNDARY PROBLEMS: APPLICATION TO DROPLET SPREADING AND SOLIDIFICATION

L. L. Zheng and H. Zhang
Department of Mechanical Engineering, State University of New York at Stony Brook, Stony Brook, NY 11794-2300, USA

A three-dimensional adaptive level set method has been developed for deformable free surface problems with or without solidification. In the new scheme, a three-dimensional multizone adaptive grid generation (MAGG) scheme is employed to track the moving boundaries and a level set method is used to capture the free surface deformation. The effectiveness and robustness of the algorithm are demonstrated by solving the droplet spreading and solidification problem, in which both free surface and solidification interface movements are important.

INTRODUCTION

Spreading and deposition of multiple splats in thermal spray processes is one of the most complex transport and phase change problems. Qualities and microstructure of the deposit are highly dependent on the rate of heat transfer and nonequilibrium kinetics of the process [1–9]. In the process, molten droplets initially impact on a substrate, and later, on top of a completely or partially solidified layer of the deposited materials. Simulation of thermal spray deposition is extremely difficult because the solidifying droplets continually deform and bond together (as well as with the substrate) to form a deposit.

Two different approaches have been widely used in simulating thermal spray processes. One is based on the interface track method in which a deforming finite element and adaptive grid scheme have been employed so that both the free surface and the solidification interface can be explicitly tracked using the Lagrangian algorithms [4]. Fukai et al. [10] have applied this scheme to the deformation of a spherical liquid metal droplet impinging on a flat surface and accounting for the presence of surface tension during the spreading process. Their results demonstrated the effects of impact velocity, droplet diameter, surface tension, and material properties on fluid dynamics of the deforming droplet. Waldvogel and Poulikakos [11] further studied the droplet configuration and flow field at the onset of phase change, as well as the final solidified shape, indicating the strong coupling between the droplet dynamics and freezing behavior. Although this approach can achieve high resolution at the interface, it is difficult to adjust grids following a highly deformed interface. When the free surfaces become highly branched, for example, two droplets merge with each other, boundary-conforming grid genera-

Received 24 June 1999; accepted 9 October 1999.
Address correspondence to Dr. Li-Li Zheng, Department of Mechanical Engineering, State University of New York at Stony Brook, Stony Brook, NY 11794-2300, USA. E-mail: lili.zheng@sunysb.edu

NOMENCLATURE

A	dimensionless area
Bo	Bond number ($= \rho g d^2/\sigma$)
C_p	specific capacity, J/kg K
d	diameter, m
F	integral function
Fr	Froude number ($= u^2/gd$)
g	square of the Jacobian; acceleration due to gravity, m/s^2
g_{ij}	covariant metric tensor
G	weight function for grid orthogonality
H	Heaviside function
I	grid characteristic
Ja	Jacobian
k	thermal conductivity, W/m K
P	pressure, Pa
Pr	Prandtl number ($= \nu/\alpha$)
$\mathbf{r}$	distance vector
Re	Reynolds number ($= ud/\nu$)
Ste	Stefan number [$= C_p(T_h - T_f)/h_f$]
s	solidified layer thickness, m
sgn	sign function
T	temperature, K
t	time, s
$\mathbf{u}$	velocity vector, m/s
u	velocity, m/s
We	Weber number ($= \rho u^2 d/\sigma$)
w	weight function
x	Cartesian coordinate, m
y	Cartesian coordinate, m
z	Cartesian coordinate, m
δ	Dirac delta function
ϵ	small value
θ	contact angle
Θ	dimensionless temperature [$= (T - T_f)/(T_h - T_f)$]
κ	curvature, 1/m
λ	positive constant
Λ	Lagrange multiplier
μ	dynamic viscosity, kg/ms
ρ	density, kg/m^3
σ	surface tension, N/m
ξ^i	curvilinear coordinates
$(x_i)_\xi$	partial derivative of (x_i) respect to ξ
ϕ	level set function

Subscripts

int	interface
k	index of interface
l	liquid
o	orthogonality or initial
s	smoothness or solid
w	weight
1, 2	fluids
ϵ	small value
ξ^i	curvilinear coordinates

tion becomes an extremely difficult task. Such cases may require rezoning or reconnection of moving grids [12–14], which is of great difficulty in a three-dimensional geometry.

The second approach is based on the volume tracking method, e.g., volume-of-fluid (VOF) scheme [7–9, 14–18], in which a finite-difference technique with fixed grid system is adopted. In contrast to the Lagrangian methods, the VOF scheme can maintain the accuracy as well as capture the free surface that undergoes arbitrarily large distortions. Liu et al. [19] studied splat formation and solidification processes using a VOF-based computer package, RIPPLE [16–18]. They considered the interaction between the free surface and solidification interface, and the interaction between two droplets impinging on a predetermined, nonflat surface [20]. Since the interface is prescribed in their studies, an interaction does not exist. Trapaga and Szekely [21] investigated the impact of a lead droplet in the absence of solidification using a three-dimensional code, FLOW-3D. Pasandideh-Fard et al. [7] further simulated the impact and solidification of tin droplets on a cold stainless steel substrate using a modified SOLA-VOF code, showing good agreement in prediction of the droplet shape in comparison with the experimental picture. Recently, researchers at the same group have extended their model to

three dimensions. Numerical simulations and experiments have been conducted for a tin droplet impacting on cold stainless steel inclined at a 45° angle [8, 9].

Besides the VOF scheme, the level set method has also been commonly used to simulate the formation and transformation of the bubbles and drops [22–25]. Adalsteinsson and Sethian [26] developed a three-dimensional level set method and applied it to simulate the topological change for the case where interface velocities are given. Further, Sussman et al. [27] developed an adaptive level set approach for modeling a water drop falling in air. Zhao et al. [28] developed a three-dimensional variational level set approach to capture the behavior of bubbles and droplet motions involving several phases. However, inertial effects were neglected in their model. Review of recent developments on level set methods can be found in Sethian [25].

Zhang et al. [29] have developed an advanced numerical scheme that combines the level set method with multizone adaptive grid generation (MAGG) and curvilinear finite-volume schemes. This scheme allowed them to take full advantage of an adaptive grid generation for accurate predictions of the moving interfaces and an interface tracking scheme for the time evolution of the free surface. Specifically, adaptive grid generation was employed to capture the solidification interface, and the level set method was used to capture the free surface evolution. This scheme has been successfully applied to various solidification problems with deformable free surfaces, demonstrating its powerful capabilities for handling very complex problems. Since this scheme was developed in two dimensions, it was incapable of describing three-dimensional behavior that often occurs during droplet spreading and solidification in thermal spray problems. To expand the capability of this scheme, we will further advance the existing MAGG [30–32] and level set formulation to three dimensions in this article. An integrated method that combines three-dimensional MAGG, a curvilinear finite-volume discretization scheme, and the level set method is proposed, together with an interface reconstruction scheme to guarantee total mass conservation. The capability of this new model is demonstrated in simulating the transport phenomena associated with moving interfaces, in particular, droplet deformation and solidification.

MATHEMATICAL FORMULATION

In the level set method, the level set function is denoted as ϕ. Initial level set function $\phi < 0$ defines one fluid and $\phi > 0$ defines the other one, and the interface of two fluids is modeled as the zero level set of ϕ. The interface movement is traced by solving a Hamilton-Jacobi type of equation in the computational domain. The signed distance from the interface is usually employed as the level set function. To model the spreading and solidification of a molten droplet, the following assumptions are made: (1) the flow is incompressible and laminar; (2) the fluids are Newtonian; and (3) the thermophysical properties are constant and uniform. The equation of the level set function can be written as follows [25]:

$$\frac{\partial \phi}{\partial t} + (\mathbf{u} \cdot \nabla)\phi = 0 \tag{1}$$

After the level set function is defined, the entire domain of interest can be treated as a single domain and the regions of various materials or phases can be distinguished by the level set function.

The governing equations for mass, momentum, and energy are then written in dimensionless form as [29]

$$\nabla \cdot \mathbf{u} = 0 \tag{2}$$

$$\frac{\partial \rho \mathbf{u}}{\partial t} + \nabla \cdot \rho \mathbf{u}\mathbf{u} = -\nabla P + \frac{1}{\mathrm{Re}} \nabla \cdot (\mu \nabla \mathbf{u}) + \frac{\rho}{\mathrm{Fr}} \mathbf{g} + \frac{\kappa}{\mathrm{We}} \delta(\phi) \nabla \phi \tag{3}$$

$$\frac{\partial (\rho C_p \Theta)}{\partial t} + \nabla \cdot (\rho C_p \mathbf{u} \Theta) = \frac{1}{\mathrm{Re\,Pr}} \nabla \cdot (k \nabla \Theta) \tag{4}$$

where $\mathbf{u}$ is the dimensionless velocity vector and Θ is the dimensionless temperature; ρ, C_p, k, and μ are the dimensionless density, specific heat, conductivity, and dynamic viscosity, respectively. Here we assume that a sharp interface exists between the two immiscible fluids with different densities ρ_1 and ρ_2, and also that the flow is incompressible, e.g., ρ_1 and ρ_2 are constant, and the diffusion between the two fluids is negligible. Furthermore, δ is the Dirac delta function, $\mathbf{g}$ is the unit gravity vector, and κ is the curvature of the free surface,

$$\kappa = -\nabla \cdot \frac{\nabla \phi}{|\nabla \phi|} \tag{5}$$

In Eqs. (3) and (4), Re, Fr, and We are the Reynolds, Froude, and Weber numbers, respectively, and are defined as $\mathrm{Re} = u_o d/\nu$, $\mathrm{Fr} = u_o^2/gd$, and, $\mathrm{We} = \rho_o u_o^2 d/\sigma$, where ρ_o, d, u_o denote the reference density, length, and velocity, respectively, and σ is the surface tension.

The last term in Eq. (3) is the surface tension effect. The delta function itself can be smoothened over several grid points using the formulation of Chang et al. [24]:

$$\delta = \begin{cases} \dfrac{1 + \cos(\pi\phi/\epsilon)}{(2\epsilon)} & \text{if } |\phi| < \epsilon \\ 0 & \text{otherwise} \end{cases} \tag{6}$$

where ϵ is a small value related to the grid space. The density and viscosity can be calculated from

$$\rho = \rho_1 + (\rho_2 - \rho_1) H(\phi) \tag{7}$$

$$\mu = \mu_1 + (\mu_2 - \mu_1) H(\phi) \tag{8}$$

where H is the Heaviside (step) function that satisfies $H(x) = 1$ for $x > 0$ and $H(x) = 0$ for $x < 0$. In the numerical simulation, the Heaviside function

$$H = \begin{cases} 0 & \text{if } \phi \le -\epsilon \\ \dfrac{\phi + \epsilon}{2\epsilon} + \dfrac{\sin(\pi\phi/\epsilon)}{2\pi} & \text{if } |\phi| < \epsilon \\ 1 & \text{if } \phi \ge \epsilon \end{cases} \tag{9}$$

is applied. The movement of the solidification interface is defined by satisfying the local energy balance. Assuming the position of the interface can be expressed as $s(x, y, z, t) = 0$, the energy balance will have the following form [33]:

$$\frac{\partial s}{\partial t} = \frac{\text{Ste}}{\text{Re Pr}}\left(\nabla\Theta_l - \frac{k_s}{k_l}\nabla\Theta_s\right) \cdot \nabla_s \tag{10}$$

where $\text{Ste} = C_{pl}(T_h - T_f)/h_f$ is the Stefan number, and h_f is the latest heat. The densities for liquid and solid are assumed to be constant and equal to each other. The above formulations are applicable for free surface problems with solidification.

NUMERICAL SCHEME

Zhang et al. [29] have developed a high-resolution computer model that combines the 2D MAGG, curvilinear finite-volume discretization, and level set method to simulate the transport phenomena associated with moving interfaces. The grid-generation scheme has been devised for fast and accurate tracking of the interface movement, as well as for clustering grids in the interface regions as the solutions progress. Next, this scheme will be further extended to three dimensions.

3D Multizone Adaptive Grid Generation

The MAGG scheme is an algorithmic procedure that orderly distributes a fixed number of grids over a physical field in a manner that some coordinate surfaces are coincident with the segments of the boundaries in the physical domain. The grid distribution in different zones is allowed to be adjusted to the solution development and the movement of the internal boundaries; the interfaces between phases are therefore preserved. The grids are generated based on a constrained adaptive optimization of grid characteristics such as smoothness, I_s, orthogonality, I_o, and weighted volume, I_w [30–32]. For the given general curvilinear coordinates, $\xi^i (i = 1, 2, 3)$, and Cartesian coordinates, $x_r (r = 1, 2, 3)$, a three-dimensional form of important grid characteristics can be written as follows:

$$I_s = \iiint \frac{1}{\sqrt{g}} \sum_i \left(g_{jj}g_{kk} - g_{jk}^2\right) d\xi^1\, d\xi^2\, d\xi^3 \qquad (i, j, k) \text{ cyclic} \tag{11}$$

$$I_w = \iiint w g\, d\xi^1\, d\xi^2\, d\xi^3 \tag{12}$$

$$I_o = \iiint \sum_i G(\mathbf{x})(g_{ij}g_{ik} - g_{ii}g_{jk})^2\, d\xi^1\, d\xi^2\, d\xi^3 \qquad (ijk) \text{ cyclic} \tag{13}$$

where w and G are weight functions that control grid volume and orthogonality, respectively. The g_{ij}'s are the elements of the covariant metric tensor,

$$g_{ij} = \mathbf{r}_{\xi^i} \cdot \mathbf{r}_{\xi^j} \tag{14}$$

where the $\mathbf{r}_{\xi^i}$'s are the three covariant base vectors of the curvilinear coordinate system, and g is the square of the Jacobian (cell volume),

$$g = \mathrm{Ja}^2 = \det | g_{ij} | \qquad (i, j, k) \text{ cyclic} \tag{15}$$

Based on the optimization approach for variational problems, the grid-generation system is then obtained as Euler-Lagrange equations by minimizing a linear combination I of the smoothness, orthogonality, and concentration, given by

$$I = I_s + \lambda_w I_w + \lambda_o I_o = \iiint F \, d\xi^1 \, d\xi^2 \, d\xi^3 \tag{16}$$

The Euler-Lagrange equations in the transformation space are

$$\frac{\partial}{\partial \xi^1} \frac{\partial F}{\partial (x_i)_{\xi^1}} + \frac{\partial}{\partial \xi^2} \frac{\partial F}{\partial (x_i)_{\xi^2}} + \frac{\partial}{\partial \xi^3} \frac{\partial F}{\partial (x_i)_{\xi^3}} - \frac{\partial F}{\partial x_i} = 0 \qquad i = 1, 2, 3 \tag{17}$$

where $(x_i)_\xi$ denotes the partial derivative of a Cartesian coordinate x_i with respect to a curvilinear coordinate ξ, and F is the kernel of the functional which is also referred to as the overall "performance function" of the optimization problem.

The grids on the interfaces are subjected to the constraints

$$f_k = f_{\mathrm{int},k}(x, y, z) = 0 \tag{18}$$

where $f_{\mathrm{int},k}$'s are known real-valued functions with respect to the arguments x, y, and z which are implicit functions of ξ, η, and ζ. They define the interfaces for constant ζ_k values, k representing the interface at different locations. The above constrained optimization problems are converted to unconstrained ones by introducing Lagrange multipliers Λ_k to form an augmented functional:

$$I = \iiint (F + \Lambda_k f_k) \, d\xi^1 \, d\xi^2 \, d\xi^3 \tag{19}$$

The Euler-Lagrange equations of the above expression together with the constraint (18) provide the necessary conditions for finding the grid distribution and Lagrange multipliers Λ_k.

The grid generator is an integrated part of the algorithm that enables the grid distribution to adapt to the solution of the transport equations. The grid movement is controlled by the values of the weight functions w and G and constants λ_o and λ_w. Finer grids are obtained where w is large and the orthogonality of the cluster grid lines is achieved when G is large. The weighting functions w and G are chosen in a similar fashion as that in two dimensions [32]. By selecting appropriate weighting functions, the grid nodes are able to be concentrated in the regions of large variations in field variables. The generated grids are usually smooth and orthogonal in the vicinity of the interface.

The boundary conditions of the equations are the position of the grid points on the domain boundaries. To move the boundary grids on a curved surface, a simple curve-fitting procedure is employed. A local surface patch is fitted to each node based on the positions of the node itself and its neighboring nodes. To fit each patch, a second-order polynomial equation of the following form is used:

$$z = Ax^2 + By^2 + Cxy + Dx + Ey + F \tag{20}$$

where the six unknown coefficients are determined from the existing surface coordinates as follows,

$$A_{i,j} = \frac{1}{2}\left[\frac{\partial^2 z}{\partial x^2}\right]_{i,j} \qquad B_{i,j} = \frac{1}{2}\left[\frac{\partial^2 z}{\partial y^2}\right]_{i,j} \qquad C_{i,j} = \frac{1}{2}\left[\frac{\partial^2 z}{\partial x \partial y}\right]_{i,j}$$

$$D_{i,j} = \left[\frac{\partial z}{\partial x}\right]_{i,j} - 2A_{i,j}x_{i,j} - C_{i,j}y_{i,j} \qquad E_{i,j} = \left[\frac{\partial z}{\partial y}\right]_{i,j} - 2B_{i,j}y_{i,j} - C_{i,j}x_{i,j} \tag{21}$$

$$F_{i,j} = z_{i,j} - \left(A_{i,j}x_{i,j}^2 + B_{i,j}y_{i,j}^2 + C_{i,j}x_{i,j}y_{i,j} + D_{i,j}x_{i,j} + E_{i,j}y_{i,j} + F_{i,j}\right) \tag{22}$$

The final finite-difference approximation of the Euler-Lagrange equations of 3D grid generation are solved by the SOR method to determine the coordinates of the grid points in a three-dimensional geometry.

Since this scheme is capable of preserving internal surfaces and always makes them coincide with grid surfaces, the interface surface is a well-defined, continuous surface and the information regarding its location, orientation, and curvature is readily available. Those values are very important for the solidification simulation. In addition, the scheme also allows grids to move adaptively as the solutions progress and/or domains change.

Combined MAGG and three-dimensional curvilinear finite-volume scheme (see Appendix) are ideally suitable to the multiphase multicomponent fluid flow problems with or without solidification. It is, however, less robust for free surface problems, especially, free surface merging and breakup. The level set formulation is, however, ideally suitable for free surface problems with or without instability. Next we will present a level set method which can be integrated with 3D multizone adaptive scheme.

Three-Dimensional Level Set Formulation

Most problems in materials processing involve convective heat and mass transfer with solidification and the free surface. The governing equations of heat and mass transfer are of elliptic type and evolving equations of the free surface are hyperbolic in nature. A different solution procedure is required for the level set function. In this article, a 3D level set method is solved using the finite-difference scheme with coordinate transformation. The solution procedure for the 3D level

set formulation is similar to that in 2D. The equations are solved by a second-order ENO scheme [34] to reduce the numerical diffusion on the free surface. The free surface is updated based on the zero set of the function and the surface tension is taken into account by adding a singular Delta function in the momentum equation [24]. Initially, the level set function is set as a signed distance from the interface. In the case of computations for large times, it does not remain a distance function at later times, and therefore, reinitialization is a critical step in the implementation of the level set method. Another important issue is the mass conservation. Numerical discretization of the level set formulation does not guarantee mass conservation even with the above reinitialization procedure. To overcome this difficulty, a second reinitialization procedure has been employed to preserve the total mass (both liquid and solid phases) in time [29].

A reinitialization procedure as proposed by Sussman et al. [27] is therefore used here, which is capable of keeping ϕ as a signed distance from the front at all times. This is accomplished by solving the following equation to steady state:

$$\frac{\partial \phi}{\partial t} = \mathrm{sgn}(\phi_o)(1 - |\nabla \phi|) \tag{23}$$

where "sgn" is the sign function. The solution of ϕ will have the same sign and the same zero level set as ϕ_o, and will satisfy $|\nabla \phi| = 1$. It is therefore a distance function from the front. Since the initial guess is often close to the signed-distance function, only a few iterations are required to obtain convergence, at least for the class of problems considered here.

Even with the above reinitialization procedure, the loss of mass may occur and the predication of the interface topography can degrade [35]. Therefore, a second reinitialization procedure is devised with a goal to preserve the global mass at each time step. This requires the solution of the following equation to steady state:

$$\frac{\partial \phi}{\partial t} + [A_o(t) - A(t)](-P + \kappa)|\nabla \phi| = 0 \tag{24}$$

$$\phi(\mathbf{x}, 0) = \phi_0(\mathbf{x}) \tag{25}$$

where $A_o(t)$ is the total liquid mass after solidification or evaporation, which can be calculated based on the total mass balance and the movement of the solidification interface; $A(t)$ is the total mass corresponding to the level set function $\phi(t)$. P is a positive constant, which helps stabilize this reinitialization procedure. Here, we have considered a stringent convergence criterion of 0.01%, which guarantees that the global mass conservation within 0.01%.

The understanding of physical conditions occurring along contact lines, i.e., where the interface comes into contact with a solid surface, is not complete. One usually has a choice of (1) a fixed contact line condition, (2) a fixed contact angle condition, or (3) a mixed condition involving the previous two cases [36–38]. Due to the dynamic nature of spreading, (2) and (3) have been used. The effects of wall adhesive at fluid interfaces in contact with rigid boundaries in equilibrium can be estimated easily within the framework of the volumetric surface force model in

terms of θ_{eq}, the equilibrium contact angle between the fluid and the wall. The angle θ_{eq} is called the static contact angle because it is measured experimentally when the fluid is at rest. The equilibrium contact angle is not simply a material property of the fluid. It depends also on the smoothness and geometry of the wall. Wall adhesion boundary conditions are more complex when the contact line is in motion, i.e., when the fluid in contact with the wall is moving relative to the wall. The equilibrium boundary condition may have to be generalized by replacing θ_{eq} with a dynamic contact angle, θ_d, which depends on local fluid and wall conditions [16].

After the level set function is obtained, the entire fluid domain including the free surface(s) can be treated as one zone. Regions of various fluids can be distinguished by the level set function. The MAGG and curvilinear finite-volume scheme are then used to solve the convection-diffusion equations. The model uses a generalized governing equation for transient processes involving diffusion and convection, thereby allowing a single formulation for the entire computational domain with or without phase change.

RESULTS AND DISCUSSION

To demonstrate the applicability and robustness of the numerical scheme based on the combined use of the level set method and MAGG, droplet spreading and solidification problems have been considered in this article. The droplet spreading and solidification is one of the most complex transport and phase-change problems [4, 6, 10, 20]. Modeling of this process is extremely difficult since both free surface and solidification interface move simultaneously and the mass in the liquid phase is continuously decreased. The schematic of the process is shown in Figure 1.

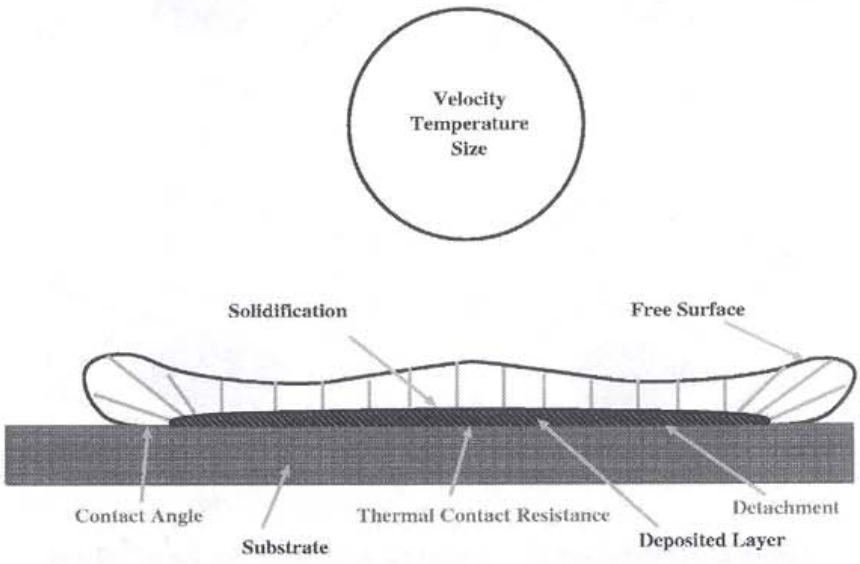

Figure 1. Schematic of an intermediate stage of a droplet deposition.

In each simulation, adaptive grid generation is used to obtain initial grids and adapt these grids with the movement of the phase-change interface, if applicable. The deformation of the free surfaces(s) is captured by the curvilinear level set formulation. An adaptive mesh of $64 \times 64 \times 32$ nodes has been used for most simulations. The parameters used guarantee that grid-independent results have been obtained. For parameters of the industrial thermal spray application, a much higher Reynolds number should be used in which a fine mesh is required. However, the primary goal here is to demonstrate the applicability of the numerical scheme, not to perform the parametric study.

Figure 2 shows that the time evolution of the free surface of a single droplet impinging vertically on a flat surface with $\mathrm{Re} = 100$ and $\mathrm{Fr} = 2.5$. The thickness of the splat is thinner at the center and thicker on the outer ring. The equilibrium contact angle of 10° has been used in the simulation. The results are almost two-dimensional, and results compare well with two-dimensional results obtained by SOLA-VOF software [6]. Figure 3 shows the results of a similar case with the gravity direction of 45° away from the z direction, e.g., the droplet is impacting on a 45° incline surface. Three-dimensional evolutions of the free surface have been shown in the figure.

The results of a droplet spreading and solidification are shown in Figure 4 for a molybdenum droplet impacting on a cold substrate of the same material. The initial position of the droplet is located at one diameter above the substrate. The Reynolds number of 5,000 with initial temperature of 100°C higher than the freezing temperature and an initial substrate temperature of 200°C have been used. Radiative cooling on the bottom of the substrate has been used. The shape of

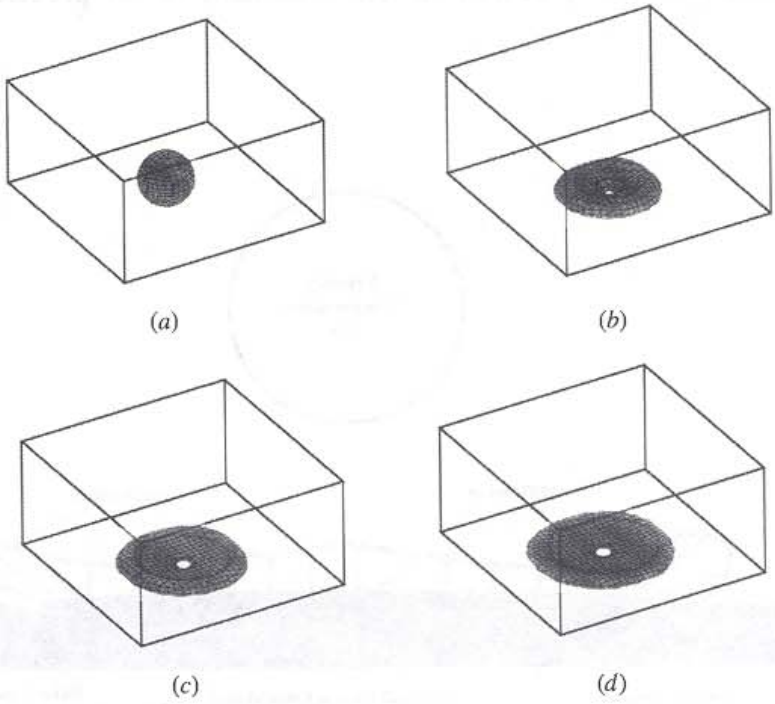

Figure 2. 3D spreading of a droplet on a substrate for $\mathrm{Re} = 100$ and $\mathrm{Fr} = 2.5$ at $t = 0.0125$, 0.025, 0.0375, and 0.05.

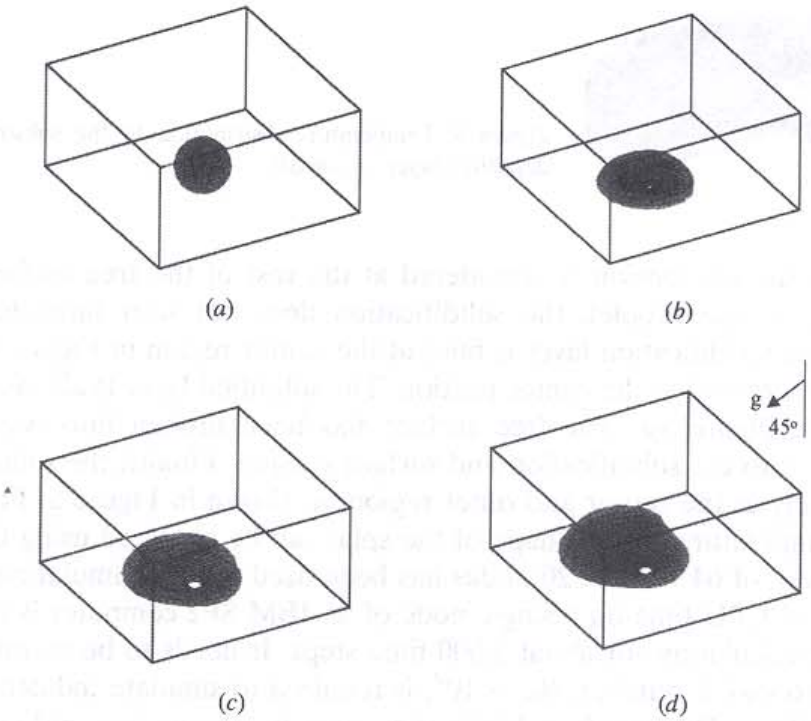

Figure 3. 3D spreading of a droplet on an incline substrate for Re = 100 and Fr = 2.5 at t = 0.0125, 0.025, 0.0375, and 0.05.

the droplet is captured by the curvilinear level set formulation with surface tension acting on the free surface, and adaptive grid generation is used to capture the solidification interface. In the simulation, the free surface is preserved between the droplet and the substrate during the impact unless the thickness is less than one grid. The no-slip boundary condition is used at the contact area, and the free

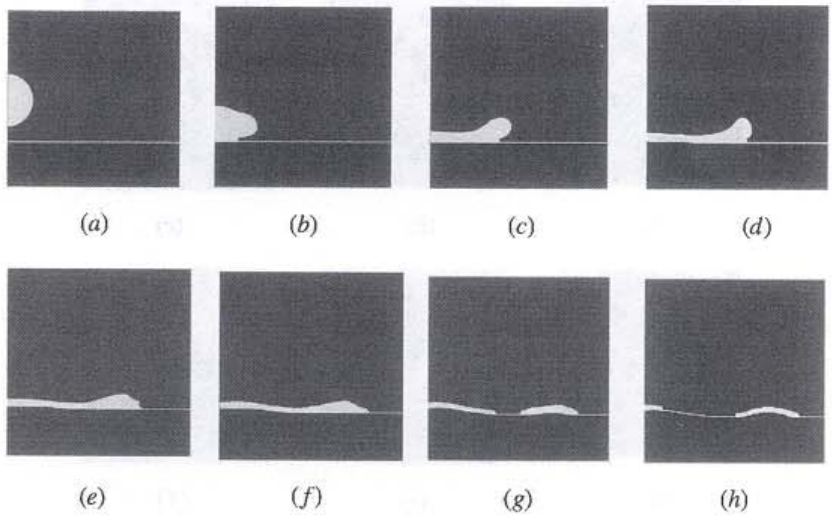

Figure 4. Spreading and solidification of a droplet on a cold substrate of the same material for Re = 5,000, Pr = 0.01, Ste_s = 0.01, Ste_l = 0.002, and We = 1,000 at t = 0.4, 0.8, 1.2, 1.6, 2.0, 2.5, 4.0, and 6.0.

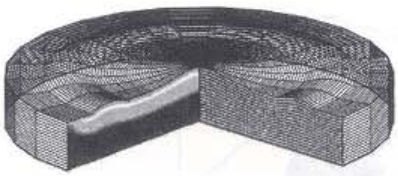

Figure 5. Temperature distribution in the substrate and the deposited layer at $t = 6.0$.

surface with surface tension is considered at the rest of the free surface. Due to superheating of the droplet, the solidification does not start immediately after impact. A thin solidification layer is built at the center region in Figure 4*e* and the thickness is increased at the center portion. The solidified layer is also found at the outer ring in Figure 4*g*. The free surface has been broken into two pieces in Figure 4*g* due to the solidification and surface tension. Finally, the solidified layer appears mainly at the center and outer region, as shown in Figure 5. For a higher substrate temperature, a disk shape of the splat can be obtained using the current model. A mesh of $64 \times 64 \times 20$ nodes has been used for this simulation. Approximately 10 h of CPU time on a single node of an IBM SP2 computer is required to perform the calculation for about 5,000 time steps. It needs to be mentioned here that a high Reynolds number, $\mathrm{Re} > 10^4$, is required to simulate industrial thermal spray deposition. This needs a highly fine grid to obtain the grid-independent results.

To study free surface instability, two sets of results are presented next. Figure 6 shows that two-dimensional free surface has been broken up due to the surface tension. In this simulation, two-dimensional surface tension has been employed neglecting the surface tension in the z direction. Therefore, only 5 nodes is sufficient in the z direction, whereas 64×64 nodes have been used in the x–y plane. In the simulation, the material 2 is placed at the central cylinder and the cylindrical ring, and the material 1 is placed in between. The cylindrical center is a

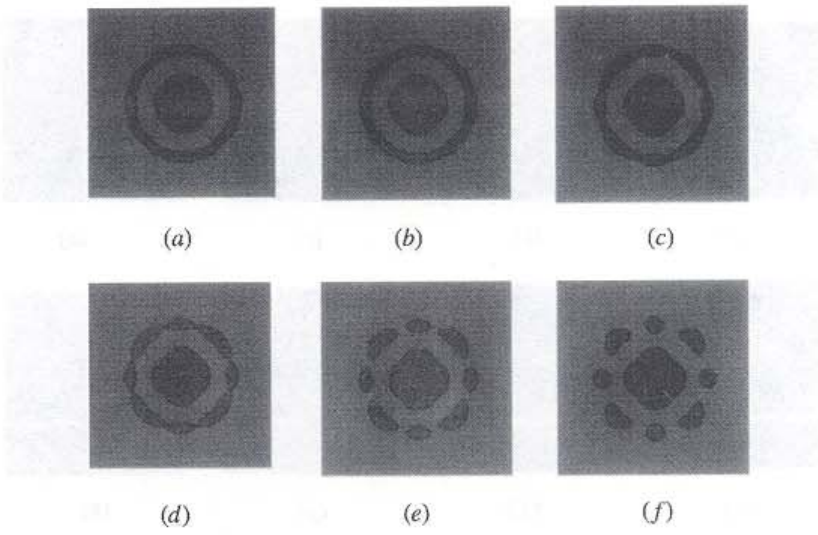

Figure 6. Droplet oscillation and breakup due to surface tension for $\rho_2/\rho_1 = 10$, $\mu_1/\mu_2 = 0.1$, and $\mathrm{Bo} = 20$ at $t = 0.04$, 0.12, 0.24, 0.32, 0.36, and 0.40.

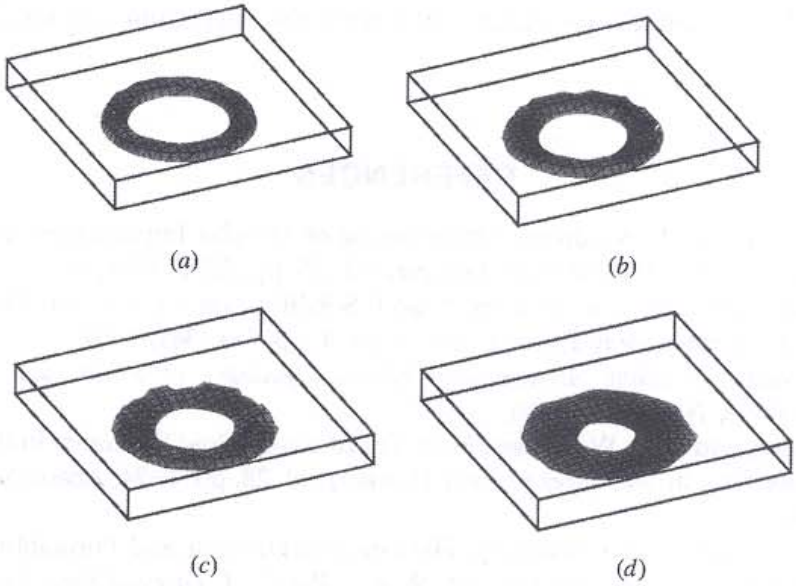

Figure 7. Droplet oscillation due to surface tension and wall interaction for $\rho_2/\rho_1 = 10$, $\mu_1/\mu_2 = 0.1$, Bo = 20, and equilibrium contact angle of 10° at $t = 0.01$, 0.10, 0.20, and 0.40.

little offset of the center of the computational domain. A perturbation will automatically be generated by this offset. The oscillatory pattern can be observed at both the inner cylinder and outer ring, while a constant volume of material 1 is trapped in between. The oscillation is enhanced at a later stage and finally the ring is broken into 8 pieces. Each piece deforms and oscillates continuously. From the results presented here together with those in Figure 4, we can conclude that the droplet may break into pieces due to the surface tension if perturbation occurs. Three-dimensional results of the surface tension instability are shown in Figure 7. The equilibrium contact angle of 10° has been assigned. At the beginning, a cylindrical ring has been placed and contacted with the bottom surface. Due to the strong surface tension between the droplet and the bottom wall, no breakup has been observed in this simulation.

CONCLUSIONS

A new free surface-capturing method is developed in three dimensions to simulate the evolution of droplet spreading with solidification. The method is based on the combination of 3D MAGG, curvilinear finite-volume approach, and level set method. In the new scheme, the grid surfaces follow the solidification surface generated by the MAGG scheme and the free surface is captured by the curvilinear level set function. This provides the capability of accurate representation of deformation, oscillation, merger, and separation of free surfaces, and phase-change interfaces. In order to account for the mass conservation during the phase-change process, a reinitialization procedure is developed based on the volume-conservation constraint. This procedure guarantees the overall total mass conservation. Numerical simulations confirm that the combined scheme can track multiple

moving interfaces/boundaries efficiently during the spreading and solidification of a droplet.

REFERENCES

1. S. Chandra and C. T. Avedisian, Observations of Droplet Impingement on a Ceramic Porous Surface, *Int. J. Heat Mass Transfer*, vol. 35, pp. 2377–2388, 1992.
2. R. C. Dykhuizen, Review of Impact and Solidification of Molten Thermal Spray Droplets, *J. Thermal Spray Technol.*, vol. 3, no. 4, pp. 351–361, 1994.
3. S. Middleman, *Modeling Axisymmetric Flows: Dynamics of Films, Jets, and Drops*, Academic Press, New York, 1995.
4. D. Poulikakos and J. M. Waldvogel, Heat Transfer and Fluid Dynamics in the Process of Spray Deposition, in *Advances in Heat Transfer*, vol. 28, pp. 1–74, Academic Press, New York, 1996.
5. V. V. Sobolev and J. M. Guilemany, Flattening of Droplets and Formation of Splats in Thermal Spraying: A Review of Recent Work—Part 1, *J. Thermal Spray Technol.*, vol. 8, pp. 87–101, 1999.
6. H. Zhang, Theoretical Analysis of Spreading and Solidification of Molten Droplet during Thermal Spray Deposition, *Int. J. Heat Mass Transfer*, vol. 42, pp. 2499–2508, 1999.
7. M. Pasandideh-Fard, R. Bhola, S. Chandra, and J. Mostaghimi, Deposition of Tin Droplets on a Steel Plate: Simulations and Experiments, *Int. J. Heat Mass Transfer*, vol. 41, pp. 2929–2945, 1998.
8. M. Bussmann, J. Mostaghimi, and S. Chandra, On a Three-Dimensional Volume Tracking Method of Droplet Impact, *Phys. Fluids*, vol. 11, pp. 1406–1417, 1999.
9. M. Pasandideh-Fard, J. Mostaghimi, and S. Chandra, On a Three-Dimensional Model of Free Surface Flows with Heat Transfer and Solidification, *Proc. 3rd ASME/JSME Joint Fluids Eng. Conf.*, *FEDSM99-7112*, San Francisco, CA, July 1999.
10. J. Fukai, Y. Shiiba, T. Yamamoto, O. Miyatake, D. Poulikakos, C. M. Megaridis, and Z. Zhao, Wetting Effects on the Spreading of a Liquid Droplet Colliding with a Flat Surface: Experiment and Modeling, *Phys. Fluids*, vol. 7, pp. 236–247, 1995.
11. J. M. Waldvogel and D. Poulikakos, Solidification Phenomena in Picoliter Size Solder Droplet Deposition on a Composite Substrate, *Int. J. Heat Mass Transfer*, vol. 40, pp. 295–309, 1997.
12. J. M. Floryan and H. Rasmussen, Numerical Methods for Viscous Flows with Moving Boundaries, *Appl. Mech. Rev.*, vol. 42, no. 12, pp. 323–341, 1989.
13. J. H. Ferziger and M. Peric, *Computational Methods for Fluid Dynamics*, 2d ed., Springer, New York, 1999.
14. R. Scardovelli and S. Zaleski, Direct Numerical Simulation of Free-Surface and Interfacial Flow, *Annu. Rev. Fluid Mech.*, vol. 31, pp. 567–603, 1999.
15. C. W. Hirt and B. D. Nichols, Volume of Fluid (VOF) Methods for the Dynamics of Free Boundaries, *J. Comput. Phys.*, vol. 39, pp. 201–225, 1981.
16. D. B. Kothe, R. C. Mjolsness, and M. D. Torrey, RIPPLE: A Computer Program for Incompressible Flows with Free Surfaces, Los Alamos Natl. Lab. Tech. Rep. LA-12007-MS, Los Alamos, NM, 1991.
17. J. U. Brackbill, D. B. Kothe, and C. Zemach, A Continuum Method for Modeling Surface-Tension, *J. Comput. Phys.*, vol. 100, pp. 335–354, 1992.
18. D. B. Kothe, W. C. Rider, S. J. Mosso, J. S. Brock, and J. L. Hochstein, Volume Tracking of Interfaces Having Surface Tension in Two and Three Dimensions, AIAA Paper 96-0859, 34th Aerospace Sciences Meeting and Exhibit, Reno, NV, 1996.

19. H. Liu, E. J. Lavernia and R. H. Rangel, Numerical Simulation of Substrate Impact and Freezing of Droplets in Plasma Spray Processes, *J. Phys. D, Appl. Phys.*, vol. 26, pp. 1900–1908, 1993.
20. H. Liu, E. J. Lavernia, and R. H. Rangel, Modeling of Molten Droplet Impingement on a Non-Flat Surface, *Acta Metall. Mater.*, vol. 43, pp. 2053–2072, 1995.
21. G. Trapaga and J. Szekely, Mathematical Modeling of the Isothermal Impingement of Liquid Droplets in Spraying Processes, *Metall. Trans.*, vol. 22B, pp. 901–914, 1991.
22. S. Osher and J. A. Sethian, Fronts Propagating with Curvature-Dependent Speed: Algorithms Based on Hamilton-Jacobi Formulations, *J. Comput. Phys.*, vol. 79, pp. 12–49, 1988.
23. M. Sussman, P. Smereka, and S. Osher, A Level Set Approach for Computing Solutions to Incompressible Two-Phase Flow, *J. Comput. Phys.*, vol. 114, pp. 146–159, 1994.
24. Y. C. Chang, T. Y. Hou, B. Merriman, and S. Osher, A Level Set Formulation of Eulerian Interface Capturing Methods for Incompressible Fluid Flows, *J. Comput. Phys.*, vol. 124, pp. 449–464, 1996.
25. J. A. Sethian, *Level Set Methods and Fast Marching Methods*, Cambridge University Press, Cambridge, U.K., 1999.
26. D. Adalsteinsson, and J. A. Sethian, The Fast Construction of Extension Velocities in Level Set Methods, *J. Comput. Phys.*, vol. 148, pp. 2–22, 1999.
27. M. Sussman, A. S. Almgren, J. B. Bell, P. Colella, L. H. Howell, M. L. Welcome, An Adaptive Level Set Approach for Incompressible Two-Phase Flows, *J. Comput. Phys.*, vol. 148, pp. 81–124, 1999.
28. H.-K. Zhao, B. Merriman, S. Osher, and L. Wang, Capturing the Behavior of Bubbles and Drops Using the Variational Level Set Approach, *J. Comput. Phys.*, vol. 143, pp. 495–518, 1998.
29. H. Zhang, L. L. Zheng, V. Prasad, and T. Y. Hou, A Curvilinear Level Set Formulation for Deformable Free Surface Problems with Application to Solidification, *Numer. Heat Transfer B*, vol. 34, pp. 1–20, 1998.
30. J. U. Brackbill and J. S. Saltzman, Adaptive Zoning for Singular Problems in Two Dimensions, *J. Comput. Phys.*, vol. 46, pp. 342–368, 1982.
31. Z. U. A. Warsi and J. F. Thompson, Application of Variational Methods in the Fixed and Adaptive Grid Generation, *Comput. Math. Appl.*, vol. 19, nos. 8/9, pp. 31–41, 1990.
32. H. Zhang and M. K. Moallemi, A Multizone Adaptive Grid Generation Technique for Simulation of Moving and Free Boundary Problems, *Numer. Heat Transfer B*, vol. 27, pp. 255–276, 1995.
33. H. Zhang and M. K. Moallemi, Numerical Simulation of Hot-Dip Metallic Coating Process, *Int. J. Heat Mass Transfer*, vol. 38, pp. 241–257, 1995.
34. A. Harten, B. Engquist, S. Osher, and S. Chakravarthy, Uniformly High-Order Accurate Essentially Nonoscillatory Schemes, III, *J. Comput. Phys.*, vol. 71, pp. 231–303, 1987.
35. W. J. Rider and D. B. Kothe, Stretching and Tearing Interface Tracking Methods, AIAA 95-1717, 12th AIAA CFD Conf., San Diego, CA, 19–22 June 1995.
36. V. E. B. Dussan, On the Spreading of Liquids on Solid Surfaces: Static and Dynamic Contact Lines, *Annu. Rev. Fluid Mech.*, vol. 11, pp. 371–400, 1979.
37. C. D. Stow and M. G. Hadfield, An Experimental Investigation of Fluid Flow Resulting from the Impact of a Water Drop with an Unyielding Dry Surface, *Proc. R. Soc. Lond. A*, vol. 373, pp. 419–441, 1981.
38. P. Haley and M. J. Miksis, The Effect of the Contact Line on Droplet Spreading, *J. Fluid Mech.*, vol. 223, pp. 57–81, 1991.
39. W. Shyy, *Computational Modeling for Fluid Flow and Interfacial Transport*, Elsevier, New York, 1994.

40. L. L. Zheng and H. Zhang, Three-Dimensional Simulation of Side Jet Thermal and Flows Mixing in Nuclear Cooling Systems, *Proc. 5th Int. Conf. Nuclear Engineering*, Nice, France, 1997, ICONE 97-2014, pp. 1–9, ASME, New York, 1997.
41. H. Zhang, V. Prasad, and M. K. Moallemi, A Numerical Algorithm Using Multizone Grid Generation for Multiphase Transport Processes with Moving and Free Boundaries, *Numer. Heat Transfer B*, vol. 29, pp. 399–421, 1996.

APPENDIX: THREE-DIMENSIONAL CURVILINEAR FINITE-VOLUME SCHEME

A three-dimensional curvilinear finite-volume solution procedure is presented here in conjunction with adaptive grid generation. The generalized Navier-Stokes equation for ϕ can be written as

$$\frac{\partial \rho \phi}{\partial t} + \frac{\partial}{\partial x_k}(J_k) = S_\phi \tag{26}$$

where ϕ is a variable, S_ϕ is the source term associated with this variable, and J_k is the flux term. J represents the transport of ϕ due to convection and diffusion and is given by

$$J_k = \rho u_k \phi - \Gamma_\phi \frac{\partial \phi}{\partial x_k}$$

and Γ_ϕ is the diffusion coefficient of ϕ. By integrating the conservation equation over a finite volume in the physical domain (Figure 8), the conservation equation in a generalized coordinate system $\xi^i (i = 1, 2, 3)$ for a typical primary point P with $\Delta\xi = \Delta\eta = \Delta\zeta = 1$ can be written as [39, 40]

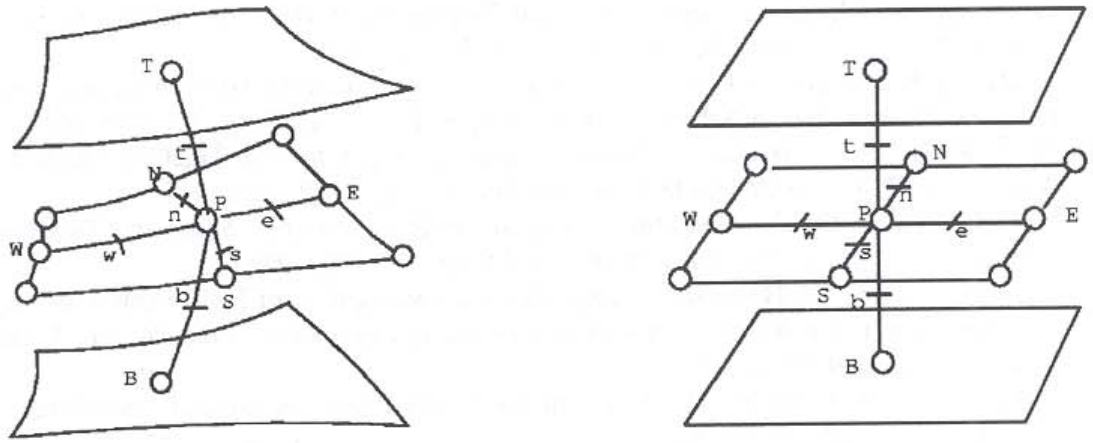

Figure 8. Schematic of the finite volume grid (*a*) in the physical domain and (*b*) in the computational domain.

$$\frac{(\rho\phi)_P^n - (\rho\phi)_P^{n-1}}{\Delta t}\,\mathrm{Ja} + (\alpha_\xi J_\xi + \beta_\xi J_\eta + \gamma_\xi J_\zeta)_e - (\alpha_\xi J_\xi + \beta_\xi J_\eta + \gamma_\xi J_\zeta)_w$$
$$+(\alpha_\eta J_\eta + \beta_\eta J_\zeta + \gamma_\eta J_\xi)_n - (\alpha_\eta J_\eta + \beta_\eta J_\zeta + \gamma_\eta J_\xi)_s + (\alpha_\zeta J_\zeta + \beta_\zeta J_\xi + \gamma_\zeta J_\eta)_t$$
$$-(\alpha_\zeta J_\zeta + \beta_\zeta J_\xi + \gamma_\zeta J_\eta)_b = (S \cdot \mathrm{Ja})_P \tag{27}$$

where the subscripts e, w, n, s, t, and b indicate the surfaces at each cell and the superscript n represents the current time step. The geometry coefficients α, β, and γ are as follows:

$$\alpha_\xi = h_\xi \sum_{i=1}^{3} C_{i1}^2/\mathrm{Ja} \qquad \beta_\xi = h_\eta \sum_{i=1}^{3} C_{i1}C_{i2}/\mathrm{Ja} \qquad \gamma_\xi = h_\zeta \sum_{i=1}^{3} C_{i1}C_{i3}/\mathrm{Ja}$$

$$\alpha_\eta = h_\eta \sum_{i=1}^{3} C_{i2}^2/\mathrm{Ja} \qquad \beta_\eta = h_\zeta \sum_{i=1}^{3} C_{i2}C_{i3}/\mathrm{Ja} \qquad \gamma_\eta = h_\xi \sum_{i=1}^{3} C_{i2}C_{i1}/\mathrm{Ja}$$

$$\alpha_\zeta = h_\zeta \sum_{i=1}^{3} C_{i3}^2/\mathrm{Ja} \qquad \beta_\zeta = h_\xi \sum_{i=1}^{3} C_{i3}C_{i1}/\mathrm{Ja} \qquad \gamma_\zeta = h_\eta \sum_{i=1}^{3} C_{i3}C_{i2}/\mathrm{Ja}$$

where

$$C_{11} = y_\eta z_\zeta - y_\zeta z_\eta \qquad C_{12} = y_\zeta z_\xi - y_\xi z_\zeta \qquad C_{13} = y_\xi z_\eta - y_\eta z_\xi$$
$$C_{21} = z_\eta x_\zeta - z_\zeta x_\eta \qquad C_{22} = z_\zeta x_\xi - z_\xi x_\zeta \qquad C_{23} = z_\xi x_\eta - z_\eta x_\xi$$
$$C_{31} = x_\eta y_\zeta - x_\zeta y_\eta \qquad C_{32} = x_\zeta y_\xi - x_\xi y_\zeta \qquad C_{33} = x_\xi y_\eta - x_\eta y_\xi$$

Introducing the fluxes J at cell surfaces, the discretized equation is then given by

$$a_P\phi_P = a_E\phi_E + a_W\phi_W + a_N\phi_N + a_S\phi_S + a_T\phi_T + a_B\phi_B + b \tag{28}$$

where

$$a_E = D_e A(\mathrm{Pe}_e)\alpha_{\xi,e} \qquad a_W = D_w A(-\mathrm{Pe}_w)\alpha_{\xi,w} \qquad a_N = D_n A(\mathrm{Pe}_n)\alpha_{\eta,n}$$
$$a_S = D_s A(-\mathrm{Pe}_s)\alpha_{\eta,s} \qquad a_T = D_t A(\mathrm{Pe}_t)\alpha_{\zeta,t} \qquad a_B = D_b A(-\mathrm{Pe}_b)\alpha_{\zeta,b}$$

$$a_P = \Sigma a_{nb}\phi_{nb} + \frac{\rho^n}{\Delta t}\mathrm{Ja}\; b = S_c\,\mathrm{Ja} + \frac{(\rho\phi)^{n-1}}{\Delta t}\,\mathrm{Ja} + b_{ex} + b_{NO}$$

$$b_{ex} = (\alpha_\xi \rho u_\xi)_w\phi_P - (\alpha_\xi \rho u_\xi)_e\phi_P + (\alpha_\eta \rho u_\eta)_s\phi_P$$
$$-(\alpha_\eta \rho u_\eta)_n\phi_P + (\alpha_\zeta \rho u_\zeta)_b\phi_P - (\alpha_\zeta \rho u_\zeta)_t\phi_P$$

$$b_{NO} = (\beta_\xi J_\eta + \gamma_\xi J_\zeta)_w - (\beta_\xi J_\eta + \gamma_\xi J_\zeta)_e + (\beta_\eta J_\zeta + \gamma_\eta J_\xi)_s$$
$$-(\beta_\eta J_\zeta + \gamma_\eta J_\xi)_n + (\beta_\zeta J_\xi + \gamma_\zeta J_\eta)_b - (\beta_\zeta J_\xi + \gamma_\zeta J_\eta)_t$$

where $D_e = \Gamma_e/h_{\xi,e}$ and $\mathrm{Pe}_e = (\rho u)_{\xi,e} h_{\xi,e}/\Gamma_e$. The same calculations are applied to D and Pe in other directions.

The expression of the pressure-correction equation depends largely on the choice of primary velocity components and the grid arrangement. In our derivation, the Cartesian velocity components are assigned as the primary variables. u_i $(i = 1, 2, 3)$ represent the velocity components in the Cartesian coordinate x^i $(i = 1, 2, 3)$. From the discretization of the momentum equations, the Cartesian velocity components can be written as follows (with the underrelaxation expressed explicitly) [41]:

$$u_{i_P} = (H_{u_i})_P + (1 - \omega)u_{i_P}^{k-1} - \frac{\omega}{a_P}\frac{\partial p}{\partial x^i} \qquad i = 1, 2, 3 \tag{29}$$

where $H_{u_i} = \omega(\Sigma a_{nb}^{u_i} u_{i,nb} + b_{u_i})/a_P$. In this equation, ω is the underrelaxation factor and the superscript $(k - 1)$ denotes the previous iteration level. The momentum equations for the covariant velocity components at the control-volume faces are obtained through algebraic manipulation of the momentum equations to yield

$$\begin{aligned}(u_\xi)_e &= (H_\xi)_e + \left(\overline{\frac{\omega}{a_P h_\xi}}\right)_e (p_P - p_E) + (1 - \omega)\left(u_\xi^{k-1}\right)_e \\ (u_\xi)_w &= (H_\xi)_w + \left(\overline{\frac{\omega}{a_P h_\xi}}\right)_w (p_W - p_P) + (1 - \omega)\left(u_\xi^{k-1}\right)_w\end{aligned} \tag{30}$$

where

$$H_\xi = \left(\frac{\partial x^1}{\partial \xi}\overline{H}_{u^1} + \frac{\partial x^2}{\partial \xi}\overline{H}_{u^2} + \frac{\partial x^3}{\partial \xi}\overline{H}_{u^3}\right)/h_\xi$$

Similarly, the $(u_\eta)_n$, $(u_\eta)_s$, $(u_\zeta)_t$, and $(u_\zeta)_b$ are obtained. $\overline{H}_{u_1}$ and $\overline{(\omega/a_P/h_\xi)}$ can be calculated by linear interpolation or more accurate interpolation schemes.